Design, Modeling and Control of a Two Flight Mode Capable Single Wing Rotorcraft With Mid-Air Transition Ability

Hitesh Bhardwaj, Xinyu Cai, Shane Kyi Hla Win, and Shaohui Foong, *Member, IEEE*

***Abstract*—Monocopters are nature-inspired, single-wing, rotating aerial vehicles that fly by spinning their entire body. Meanwhile, bicopters are twin propeller-based aerial vehicles that control their attitude by changing the direction of thrust from the motors using two servos. In this paper, we present a novel single-wing aerial vehicle, which can fly in both the monocopter and bicopter modes. To enhance its maneuverability while still being in the air, the platform can perform a mid-air transition from one mode to another. To achieve this, we fused the attributes of monocopter and bicopter, while allowing the monocopter to maintain its natural shape for flight. Considering forces and torques experienced by both modes of flight, the dynamics are described, and a cascaded control strategy is developed. A novel approach is proposed to control the angular velocity of the monocopter. An innovative blending and transition method of controllers for both modes is developed to allow transition between the two modes. We constructed a prototype to demonstrate the flight of the aerial vehicle in both modes. The results verify the proposed concept for the design of the aerial vehicle, along with the control strategy implemented for the control over the states during the flight modes as well as the transition between the two modes.**

***Index Terms*—Aerial systems: applications, aerial systems: mechanics and control, biologically-inspired robots.**

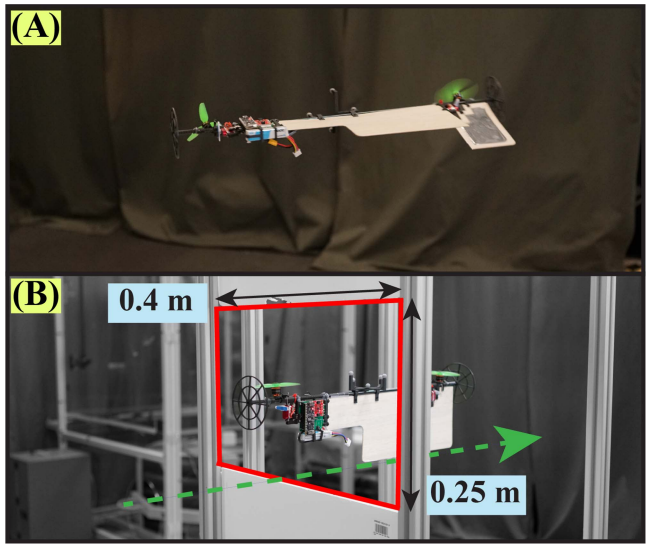

Fig. 1. Picture of our prototype flying - (A) in monocopter mode (B) through a narrow gap in bicopter mode.

I. Introduction

UNMANNED Aerial Vehicles (UAVs) have been continuously gaining attention since their development, owing to the multitude of tasks they can accomplish involving mapping, inspection, and observation. In the past, research has enhanced the performance and capabilities of traditional UAVs through additional flight modes. An additional flight mode can help accomplish different objectives using a single platform. In [1], the authors have proposed a tri-tiltrotor UAV, which can perform a conversion between vertical take-off and landing, and fixed-wing flight modes. In [2], the authors presented a transformable hovering rotorcraft, which can achieve controllability in 4 degrees of freedom while in horizontal cruising mode and 5 degrees of freedom while in its hovering mode. In [3], the authors have introduced a flying robot that can roll over on the ground, through a gap that is narrower than its diameter.

Monocopters are single-wing rotating aerial vehicles, which achieve lift by spinning around the yaw axis (Fig. 1(A)). The inspiration for the monocopters has been taken from maple seeds (or samaras) which can utilize their shape to auto-rotate while falling. So far, the monocopter platform has been used for different applications where spinning nature can be utilized. Work done in [4] shows an example of an unpowered monocopter-based lightweight sensor, that can achieve a soft landing due to its shape. Alongside soft landing, the concept of autorotation has also been explored for directional control while in descent using a control surface such as an aileron or flap in [5], [6]. Together with a flap for directional control, monocopters can utilize a motor-driven propeller to achieve lift for the ascent. Works done in [7] and [8] are examples where this principle has been applied. A recent study conducted in [9] tried to study the dynamics of the monocopters having multiple actuators to achieve better position control. In [10], the authors have presented a monocopter-based platform for short-range

Manuscript received 24 February 2022; accepted 26 July 2022. Date of publication 9 September 2022; date of current version 16 September 2022. This letter was recommended for publication by Associate Editor B. Duncan and Editor P. Pounds upon evaluation of the reviewers' comments. *(Corresponding author: Shaohui Foong.)*

The authors are with the Engineering Product Development Pillar, Singapore University of Technology & Design, Singapore 487372 (e-mail: hitesh_bhardwaj@mymail.sutd.edu.sg; xinyucai2-c@my.cityu.edu.hk; hlawin_kyi@alumni.sutd.edu.sg; shao@sutd.edu.sg).

This letter has supplementary downloadable material available at https://doi.org/10.1109/LRA.2022.3205454, provided by the authors.

Digital Object Identifier 10.1109/LRA.2022.3205454

TABLE I
COMPARISON OF MONOCOPTERS AND BICOPTERS

Parameter	Monocopters	Bicopters
Actuators	2	4
Hovering style	Spins continuously about yaw axis	Zero angular velocity in hover mode
Feedback required	Heading	Angular states
Lift generation	Single wing	Dual propellers
Take-off and landing	Spins to and from a smooth surface	Vertical take-off and landing

urban surveillance and sampling missions. A recent work done in [11] shows the development of three-dimensional electronic micro-fliers based on the platform, covering a wide variety of use case scenarios. The spinning nature of the platform also helped in passively scanning and mapping the surrounding environment using Simultaneous Localization and Mapping (SLAM) in [12]. Similarly, in [13] and [14], the authors have shown applications for the monocopter for simultaneous image and onboard state estimation and LiDAR inertial odometry, respectively.

On the other hand, a bicopter UAV uses two motors to generate collective lift force and torque in the roll axis using differential thrust. Additionally, two servos produce torque in pitch and yaw axis by tilting the motors (Fig. 1(B)). Several studies have been conducted on the bicopter platform. In [15], the authors developed a functional mini tiltrotor UAV, which, unlike the conventional tiltrotor swashplate mechanism, utilized the tilting of rotors to stabilize the UAV. In [16], the authors have presented a prototype based on research conducted on the principles of motion and the design of an attitude stabilizing controller based on a Proportional Integral Derivative (PID) controller. In [17], the authors have presented a detailed process of development of a bicopter, including an aerodynamic analysis of the propellers for optimizing the efficiency and control system design. In [18], the authors have presented a fixed pitch bicopter, which tries to utilize the gyroscopic torque for pitch response. Besides these and various other studies, the concept of bicopters has been implemented on manned aircrafts as well [19], [20], [21]. A comparison of the main characteristics of bicopters and monocopters has been presented in Table I, which highlights the differences between the two flight modes. In particular, during hover, the monocopter spins its entire body while the bicopter has zero angular velocity.

To capitalize on the advantages of the two platforms, we introduce a novel single-wing rotorcraft, that can fly in both monocopter and bicopter modes. The motivation behind using these modes for this platform is to obtain the best combination for achieving a power-efficient flight (monocopter mode), and hover with zero angular velocity (bicopter mode). The aerodynamic force produced by the wing and the rotating motion provides monocopter mode with passive stability while hovering. The ability to auto-rotate helps the mode to reduce the impact in no-power mode. Moreover, recent research has also demonstrated that the rotating wing platform has superior power efficiency compared to other platforms [22]. Monocopters can be employed for various applications where the spinning nature of the platform can be utilized, for example, passively scanning and mapping the surrounding environment as done in [12], [13]. However, even though the monocopter platform is based on a single wing, the physical footprint of the spinning drone is large enough to hinder its mobility. The platform has a highly nonlinear dynamic nature [7]. Moreover, the cost-effective sensors available in the market will struggle to measure the states of monocopter as they cannot keep up with the rotation speed of the platform. On the other hand, the flight mode of a bicopter is steady with zero angular velocity during hovering. This benefits in achieving position and attitude control with easier control effort. The steady nature of the UAV contributes to capabilities such as close inspections and steady mode video transmission. Additionally, the smaller footprint while hovering allows maneuvering through small spaces. Therefore, the combination of flight modes onto a single platform not only increases the merits but also helps to overcome each other's limitations.

The bicopter bears a resemblance to the tailsitter, which is particularly good for its efficiency in forward-flight mode, however, owing to its forward velocity, this mode is not suitable for operations inside a confined space. Furthermore, the tailsitter would simply crash during a fail-safe scenario, however, the monocopter mode can help in a softer landing, comparatively. Besides the capability to fly in two different flight modes, our platform is also able to perform a transition from one mode to another without landing. Since the two flight modes have completely different hovering styles (one being rotating and the other being steady), a blending and transition control of the two modes is required. The monocopter mode and the bicopter mode will hereafter be called the M-mode and the B-mode.

The contributions of this work are as follows:

- Design and control a rotorcraft having two different modes of flight,
- Experimental proof of successful takeoff and position control in both flight modes,
- Experimental proof of transition between two different flight modes while in flight.

II. DYNAMIC MODELING

Let $(X^{\mathcal{I}}, Y^{\mathcal{I}}, Z^{\mathcal{I}}) \in \mathcal{I}$ denote the right-handed inertial frame and $(x^{\mathcal{B}}, y^{\mathcal{B}}, z^{\mathcal{B}}) \in \mathcal{B}$ denote the body frame attached to the Centre of Gravity (CG) of the UAV as depicted in Fig. 2. The rotation angles in $X^{\mathcal{I}}$, $Y^{\mathcal{I}}$, and $Z^{\mathcal{I}}$ directions are denoted by ϕ, θ, and ψ. Using the Newton-Euler formulation, the translational dynamics of the UAV can be expressed as,

$$m\ddot{\boldsymbol{P}}^{\mathcal{I}} = \boldsymbol{R}_{\mathcal{B}}^{\mathcal{I}}\boldsymbol{F}^{\mathcal{B}} + m\boldsymbol{G} \tag{1}$$

where $\boldsymbol{P}^{\mathcal{I}} = [P_X, P_Y, P_Z]^T$ is the position vector in the inertial frame, $\boldsymbol{R}_{\mathcal{B}}^{\mathcal{I}}$ represents the rotational transformation from body-frame to inertial-frame, $\boldsymbol{F}^{\mathcal{B}} = [F_x, F_y, F_z]^T$ is the force vector, and $\boldsymbol{G} = [0, 0, g]^T$ is the gravity vector.

Similarly, the attitude dynamics equation of the UAV can be expressed as,

$$\boldsymbol{I}^{\mathcal{B}}\dot{\boldsymbol{\omega}}^{\mathcal{B}} + \boldsymbol{\omega}_{\times}^{\mathcal{B}}\boldsymbol{I}^{\mathcal{B}}\boldsymbol{\omega}^{\mathcal{B}} = \boldsymbol{\tau}^{\mathcal{B}} \tag{2}$$

where $\boldsymbol{I}^{\mathcal{B}} \in R^{3\times3}$ is the inertia matrix, $\boldsymbol{\omega}^{\mathcal{B}}$ is the angular velocity in the body frame, and $\boldsymbol{\tau}^{\mathcal{B}} = [\tau_x, \tau_y, \tau_z]^T$ is the torque vector.

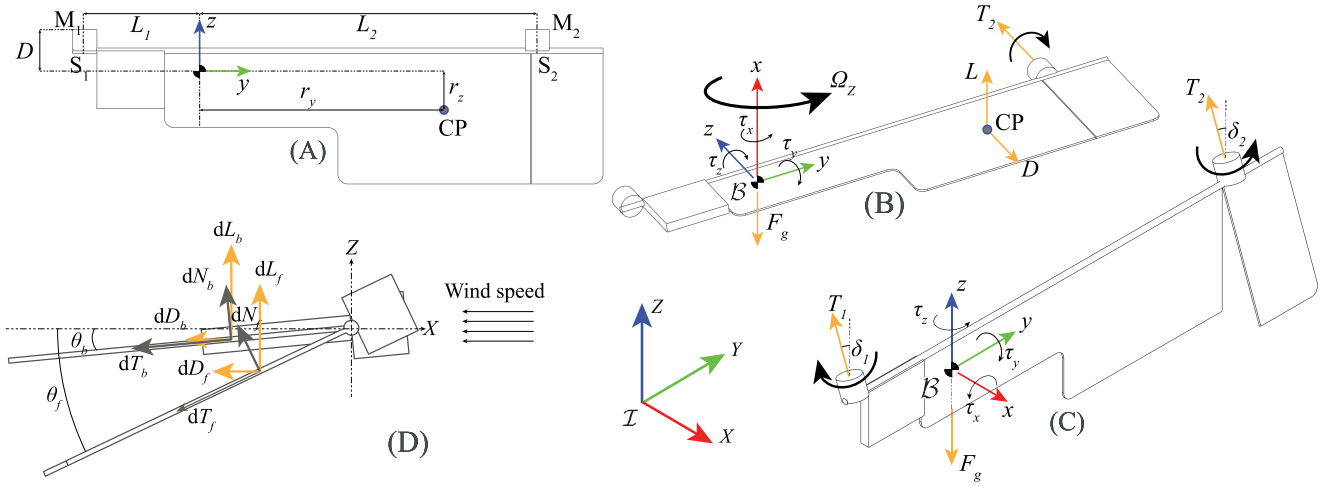

Fig. 2. (A) Top view of the UAV labeling various dimensional parameters as well as the location and number of motors (M_1, M_2) and servos (S_1, S_2). (B) Isometric view of UAV in M-mode, and (C) B-mode, labeling the forces acting in the two modes. T_1, T_2 are the thrust forces generated by motors and propellers, and δ_1 and δ_2 are the angles controlled by the servos. The rotation direction of propellers as well as the monocopter's spin direction are marked with arrows. (D) Cross-section view of the UAV, depicting the aerodynamic forces acting on the wing and the flap surfaces of the UAV where dL refers to lift force, dD refers to drag force, dN refers to normal force and dT refers to tangential force on each blade element. Subscripts b and f denote the body and flap, respectively.

The aerodynamic forces acting on the wing and flap surfaces (Fig. 2(D)) are modeled with the Blade Element Theory (BET) [23]. Under BET, a surface is sliced span-wise into n blade elements, and the overall lift and drag contributions are obtained summing up the individual contributions. Each element's lift and drag contribution can be defined as,

$$\mathrm{d}L = \frac{1}{2} C_l \rho U^2 c \mathrm{d}r, \qquad \mathrm{d}D = \frac{1}{2} C_d \rho U^2 c \mathrm{d}r \tag{3}$$

where C_l and C_d are the lift and drag coefficients respectively, ρ is the density of air, U is the relative air velocity encountered at the tip of the blade element, c is the chord length of each blade element, and dr is the width of each blade element. dL and dD can be resolved into normal and tangential forces as,

$$\mathrm{d}N = \mathrm{d}L\cos\theta + \mathrm{d}D\sin\theta, \quad \mathrm{d}T = \mathrm{d}L\sin\theta - \mathrm{d}D\cos\theta \tag{4}$$

By integrating (4), we can obtain the overall contribution of normal and tangential forces for both wing and flap which are at different angles of attack (θ_b and θ_f, respectively) with respect to the inertial frame. We assume that the total normal (N_t) and tangential (T_t) forces from wing and flap will be acting on the Centre of Pressure (CP). These forces can be calculated as,

$$\begin{bmatrix} N_t \\ T_t \end{bmatrix} = \begin{bmatrix} N_b \\ T_b \end{bmatrix} + \boldsymbol{R}_f^{\mathcal{B}} \begin{bmatrix} N_f \\ T_f \end{bmatrix} \tag{5}$$

where subscript t, b, and f refer to total, body and flap forces respectively, and $\boldsymbol{R}_f^{\mathcal{B}} \in R^{2\times 2}$ represents the rotational transformation from flap-frame to body-frame.

During the spinning motion of the UAV, a precession torque is experienced, which can be obtained by, $\boldsymbol{\tau}_{prec} = \boldsymbol{I}_p \omega_p \times \boldsymbol{\omega}$, where, $\boldsymbol{I}_p$ and ω_p is the moment of inertia and rotational speed of the propeller [24]. Considering the body frame axis definition, the first and third components obtained for $\boldsymbol{\tau}_{prec}$ will be zero, and therefore can be ignored. Using the Newton's laws and the free body diagram given in Fig. 2, the total force and moment equilibrium equations for the UAV can be written as,

$$\begin{aligned} F_x &= (T_1 \sin\delta_1)\,\alpha + T_2 \sin\delta_2 + (N_t)\,\beta, \quad F_y = 0 \\ F_z &= (T_1 \cos\delta_1)\,\alpha + T_2 \cos\delta_2 - (T_t)\,\beta \end{aligned} \tag{6}$$

$$\begin{aligned} \tau_x &= (-T_1 \cos\delta_1 L_1)\,\alpha + T_2 \cos\delta_2 L_2 - (T_t r_y - f_{drag} L_2)\,\beta \\ \tau_y &= (T_1 \sin\delta_1 D)\,\alpha + T_2 \sin\delta_2 D - (N_t r_z + \tau_{prec,2})\,\beta \\ \tau_z &= (T_1 \sin\delta_1 L_1)\,\alpha + T_2 \sin\delta_2 L_2 - (N_t r_y)\,\beta \end{aligned} \tag{7}$$

where f_{drag} is drag force induced by the propeller flying in its own wake and $\tau_{prec,2}$ is the second component of the precession torque $\boldsymbol{\tau}_{prec}$. α, $\beta \in [0, 1]$ are control parameters that can be varied to modify the dynamics of the overall system for a specific mode.

Considering the force and torque equilibrium of the UAV ((6) and (7)), and the fact that M_1 and S_1 are not used for the monocopter flight, the body force and torque equations for the UAV in M-mode can be obtained by taking $\alpha = 0$ and $\beta = 1$ in (6) and (7).

A few assumptions are made for simplification of the dynamics while flying in B-mode. (1) The lift and drag generated by the wing are considered to be negligible in steady state. (2) The reaction torques due to the servos and propellers are considered negligible as they are comparatively much smaller compared to the torque induced by the thrust in the body frame. (3) The thrust force projected by the motors is considered to be present in the x-z frame in the steady state. This force will be projected in the y-axis during the transient response but will become zero as the roll angle of the UAV converges to the commanded value by the controller. Considering these assumptions, the body force and torque equations for the UAV in B-mode can be obtained by taking $\alpha = 1$ and $\beta = 0$ in 6 and 7.

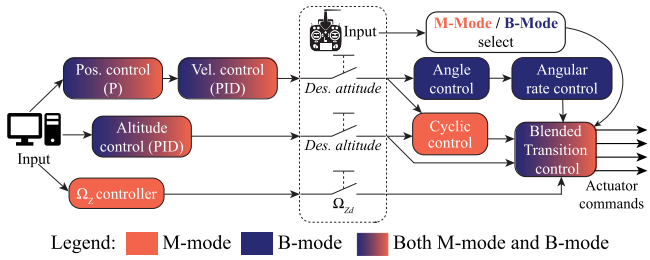

Fig. 3. Cascaded control architecture used on UAV.

III. Flight Control and Transition

The control architecture of the UAV can be divided into three main sections: (1) Monocopter control, (2) Bicopter control, and (3) Transition phase. The overall controller is based on a cascaded control strategy, where the higher-level controller controls the position in the three-axes. A manual switch can control the flight input data to be fed from a radio controller or the position, velocity, and altitude controllers as depicted in Fig. 3.

A. M-Mode Control

1) Cyclic Controller: The lower-level controller for M-mode flight is based on a cyclic controller which generates a periodic signal to steer the UAV in a specific direction. The cyclic control for the monocopter is based on the square cyclic control strategy which has been previously implemented in [25].

The monocopter constantly rotates in the Z-axis, the error for which is corrected with the altitude control based on a PID controller. The directional control correlates to the roll(ϕ_c) and pitch(θ_c) commands for position correction in X and Y directions. The direction control variable ψ_c and the amplitude of the cyclic control T_{amp} are calculated as,

$$\psi_c = \text{atan2}\left(\frac{\phi_c}{\theta_c}\right), \qquad T_{amp} = k_c\sqrt{\phi_c^2 + \theta_c^2} \tag{8}$$

where k_c is a constant to scale the effectiveness of roll and pitch actuation commands. The cyclic commanded thrust for the motor includes both the components for the altitude as well as direction and is computed as,

$$T_{cyc} = \begin{cases} u_Z + T_{amp}, & \text{if } \sin(\psi + \psi_c + \psi_0) > \epsilon \\ u_Z - T_{amp}, & \text{otherwise} \end{cases} \tag{9}$$

where u_Z is the altitude correction, ψ is the current azimuth heading of the monocopter, ψ_0 is the offset value for angular correction induced due to gyroscopic precision and other effects, and ϵ is the variable to control the duty cycle.

2) Rotational Speed Controller: Typically, a single actuator monocopter does not have control over the rate at which it is spinning. This rate of spin or the angular velocity depends on the shape, size, and weight distribution of the UAV. However, for the designed platform, the angular velocity needs to be controlled in the desired manner for better efficiency, more control authority, and to assist in the transition between modes. Therefore, using S_2, the angle of the flap and motor are controlled to provide extra lift to control the rotational speed as well as reduce the effort on the motor.

Typically, owing to the fast-spinning speed in M-mode, those force components perpendicular to the rotating axis can be treated as zero over a rotation cycle in the inertial frame as they have a limited impact on the translational motion. In the hovering state, the collective force aligned with the rotating axis balances the gravity. As a result, we can determine the equilibrium for hovering using,

$$R_{\mathcal{B}}^{\mathcal{I}}(1,:)\left[F_x, F_y, F_z\right]^T = mg, \quad \left[\tau_x, \tau_y, \tau_z\right] = \mathbf{0}. \tag{10}$$

where $R_{\mathcal{B}}^{\mathcal{I}}(1,:)$ refers to the first row of the rotation matrix, as the gravity is applied on the x-axis in M-mode (Fig. 2(B)). By solving (10), we can obtain the equilibrium of motor thrust T_2, roll angle ϕ, pitch angle θ, as well as the rotating speed Ω_z. Particularly, by choosing a different servo angle δ_2, the rotating speed Ω_z can be controlled.

B. B-Mode Control

1) Attitude Controller: The attitude controller for the B-mode flight consists of a higher-level quaternion-based controller and a lower-level angular rate controller. The inputs for the attitude controller are the UAV quaternion and the desired attitude. The quaternion-based controller is based on the work done in [26]. The higher-level controller for the attitude control can be defined as,

$$\boldsymbol{\Omega_d} = \boldsymbol{c_A}\text{sign}(q_{err_w})\boldsymbol{q_{err_{xyz}}} \tag{11}$$

where $\boldsymbol{\Omega}_d$ is the desired angular rates vector, $\boldsymbol{c_A}$ is the attitude gain vector, and $\boldsymbol{q_{err}} = \boldsymbol{q}^{-1} \cdot \boldsymbol{q_d}$ is the error quaternion. The lower-level attitude control is the angular rate controller, which is a PID control over the angular rate of the UAV given by,

$$\boldsymbol{\tau_d} = \boldsymbol{c_{p_a}}\boldsymbol{e_a} + \boldsymbol{c_{d_a}}\dot{\boldsymbol{e}}_{\boldsymbol{a}} + \boldsymbol{c_{i_a}}\int_0^t \boldsymbol{e_a}(\boldsymbol{t})\text{d}t \tag{12}$$

where $\boldsymbol{\tau_d} = [\tau_{xd}, \tau_{yd}, \tau_{zd}]^T$ is the desired moment vector, $\boldsymbol{c_{p_a}}$, $\boldsymbol{c_{d_a}}$ and $\boldsymbol{c_{i_a}}$ are the proportional, derivative, and integral gain vectors, and $\boldsymbol{e_a}$ is the angular rate error vector.

2) Control Allocation: A relationship between the attitude controller output $\boldsymbol{\tau_d}$ along with F_{zd} and the desired actuator commands (T_1, T_2, δ_1, and δ_2) can be established. Reference [17] describes an intuitive method to generate these desired actuator commands. Therefore, using (6) and (7), the actuator commands for B-mode can be calculated as,

$$T_1 = \sqrt{\frac{(\tau_{xd} - F_{zd}L_2)^2}{(L_1 + L_2)^2} + \frac{(D\tau_{zd} - L_2\tau_{yd})^2}{D^2(L_1 - L_2)^2}} \tag{13a}$$

$$T_2 = \sqrt{\frac{(\tau_{xd} + F_{zd}L_1)^2}{(L_1 + L_2)^2} + \frac{(D\tau_{zd} - L_1\tau_{yd})^2}{D^2(L_1 - L_2)^2}} \tag{13b}$$

$$\delta_1 = -\text{atan}\left(\frac{(D\tau_{zd} - L_2\tau_{yd})(L_1 + L_2)}{D(L_1 - L_2)(\tau_{xd} - F_{zd}L_2)}\right) \tag{13c}$$

$$\delta_2 = -\text{atan}\left(\frac{(D\tau_{zd} - L_1\tau_{yd})(L_1 + L_2)}{D(L_1 - L_2)(\tau_{xd} + F_{zd}L_1)}\right) \tag{13d}$$

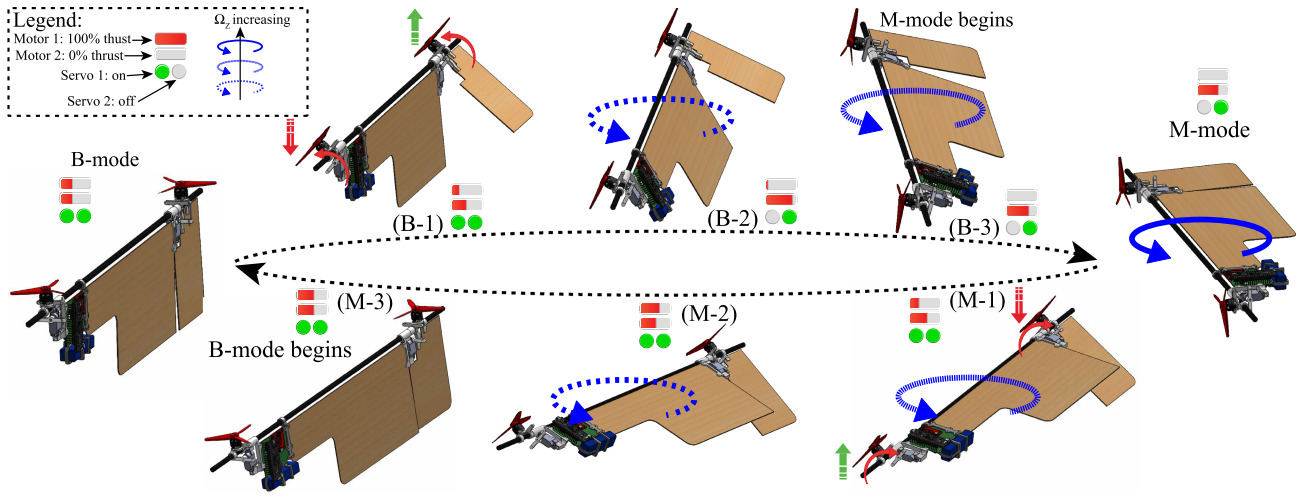

Fig. 4. Transition cycle showing the change of orientation from one mode to another. Transitioning from B-mode to M-mode following the top arrow, at stage B-1, the UAV pitches down aggressively, while simultaneously increasing and decreasing the thrust in M_2 and M_1, respectively. Due to the uneven thrust, at stage B-2, the UAV starts to gain rotational velocity. As the velocity increases, the controller is switched to M-mode in stage B-3. Transitioning from M-mode to B-mode following the bottom arrow, at stage M-1 the UAV stalls the flap to increase the pitch and decrease the rotational speed, while simultaneously increasing and decreasing the thrust in M_1 and M_2, respectively. Stalling of wing and balance of thrust in motors reduce the rotational speed further in stage M-2, while the servos start to align to desired values. At stage M-3, the controller is switched to B-mode, which takes over the control of the actuators for flight.

C. Blended Transition Control

The transition control is based on the concept of providing the best conditions for the subsequent flight mode to take over while maintaining the stability and control of the UAV in the present flight mode. One of the easiest methods for switching controllers would be using a simple on-off method, but since the two different flight modes are based on different attitude controllers, a blending strategy is imposed for handing over the control.

The transition strategy developed for the UAV is a heuristic-based design to utilize the nature of flight modes and the attitude controllers implemented. The controller is essentially a phase-in phase-out control of the two flight modes based on a sigmoid function, preceded by blending control, which is a series of movements to orientate the UAV and initiate the controller for each mode. Fig. 5 depicts the switching of controls from B to M-mode and M to B-mode respectively, illustrating the initialization of blending using the motors and servos, followed by the switching of the controllers. The sigmoid function used for controlling switching output sw_c is given by,

$$sw_c = \frac{1}{1 + e^{-(t-b)/r}} \tag{14}$$

where t is the time, and b and r are parameters used to define the offset and slope which can be changed to obtain the desired results.

Fig. 4 depicts the transition of UAV from B-mode to M-mode, showing the various stages which are encountered during the transition. To transit from B-mode to M-mode, the natural stability of the monocopter was utilized. The fact that a monocopter spins naturally on its axis when falling through the air was utilized to initiate the transition. To transit from M-mode to B-mode, the stalling of the wing plays a crucial role. This is done to subside the rotation rate as quickly as possible and to pitch up the UAV to orientate the UAV for the B-mode controller to take over.

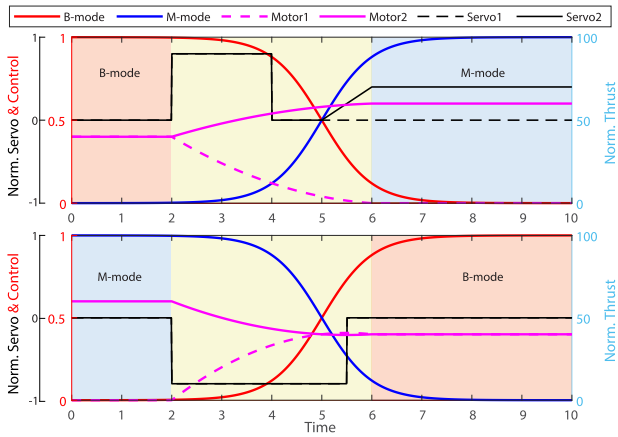

Fig. 5. An illustration of switching of controls from B to M-mode and M to B-mode, where the yellow zone marks the blending and transition of controls. The servo angles are normalized from -1 to 1. Control $= 0$ means no control and Control $= 1$ means full control. The thrust value is normalized from 0 to 100.

The transition from B-mode to M-mode starts with an aggressive pitch maneuver and simultaneous reduction of M_1 thrust. The thrust of M_1 keeps reducing as orientation changes to transit to the other mode. As the M-mode activates, the S_1 and M_1 are disabled to save battery. To transit from M-mode to B-mode, the UAV utilizes S_2 to intentionally stall the wing by reducing the rotational speed and gaining high pitch, followed by initiation of M_1 and S_1, and finally passing the control to B-mode.

IV. Experimental Results

A physical prototype of the UAV defined earlier was made for experimental verification of the model. Fig. 6 shows the UAV,

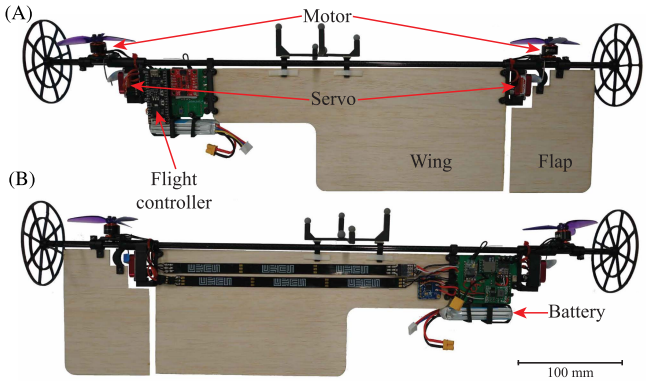

Fig. 6. Final prototype developed for experimentation depicting (A) top view and (B) bottom view.

TABLE II
TABLE OF RELEVANT VARIABLES

Parameter	M-mode	B-mode	Units
L_1, L_2, D	140, 295, 50		mm
k_c, ϵ	0.75, 0.1	-	-
γ_0	$-3\pi/2$	-	rad
$\boldsymbol{c_A}$	-	[12, 10, 10]	rad/s
$\boldsymbol{c_{p_a}}$	-	[35, 25, 20]	Nms/rad
$\boldsymbol{c_{d_a}}$	-	[0.01, 0.01, 0]	Nms^2/rad
$\boldsymbol{c_{i_a}}$	-	[0.1, 0.1, 0.3]	Nm/rad
b, r	3, 0.1	2, 0.2	-

consisting of a carbon fibre rod, 3D printed structures for holding the two servos, motors, and landing gears on each side, and a wing and flap cut from Balsa wood. Two EMax 30 A ESCs (electronic speed controllers) drive the twin TMotor 4500 KV brushless motors. Each motor is attached to a 3-inch propeller, capable of generating a maximum of 100 g of thrust, which leaves sufficient overhead for control of the UAV, which weighs 152 g in total. Using a standard 3S 300 mAh Li-Po battery, the UAV has an endurance of approximately 2.8 ± 0.2 mins while hovering in the B-mode and 3.2 ± 0.2 mins while hovering in the M-mode. An ESP32 micro-controller was used onboard, which is connected through a receiver to the transmitter for receiving the manual signal as well as through Wi-Fi to the ground station. Table II tabulates the relevant dimensional and gain parameters, along with their numerical values.

Testing of the prototype was performed to verify the following objectives: (1) Both the modes are fully operable with control over the position and attitude, and (2) In-flight transitions can be performed from one mode to another. In the experiments, along with the sensors onboard, the OptiTrack system was used to provide position and orientation data for closed-loop control.

Fig. 7 compares the power consumption of M-mode and B-mode while hovering. It was observed that during B-mode, which utilizes all actuators, the current drawn and hence the power consumed is more compared to the M-mode. On average, hovering flight in B-mode consumed approximately 50.38 W, compared to 40.45 W consumed by M-mode, making the M-mode 21.86% more efficient.

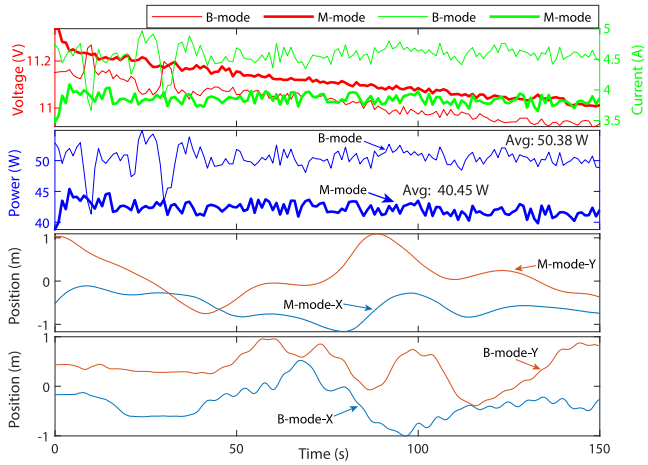

Fig. 7. Comparison of power consumption during hovering in the two modes.

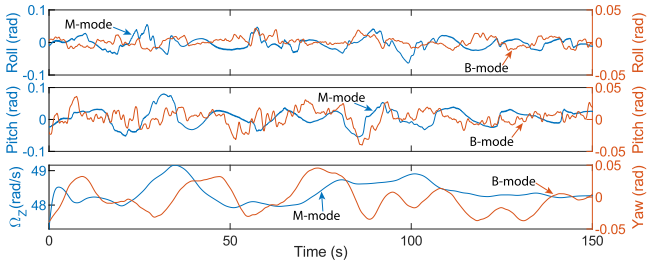

Fig. 8. Euler angles and Ω_Z during a hovering flight in M-mode and B-mode.

Fig. 8 depicts the Euler angles of the UAV during the M-mode and B-mode flight. For the M-mode flight, the roll and pitch of the UAV are varying between ± 0.1 rad, indicating the effort to hold the position using the cyclic control implemented. Fig. 8 also depicts the Ω_Z for M-mode flight, which is controlled by the rotational speed controller. On the other hand, the roll, pitch, and yaw values for the B-mode flight fluctuate only between ± 0.05 rad, depicting more stability during hovering.

A. Position Tracking

Using the controllers mentioned, the UAV was commanded to fly towards waypoints forming a square pattern and fly in a circular path to follow a trajectory. Figs. 9(A) and 10(A) depict the desired and actual position of the UAV along with the actuator output while following the waypoints and while tracking the trajectory, respectively, for the M-mode flight. From the figures, it can be observed that altitude control is very responsive and stable, due to the direct control of the motor over the Z-axis. The position control, however, is hindered by the nonlinear nature of the platform. A slower response is observed because of indirect control and due to the gyroscopic nature of the UAV. One way to solve this issue is by implementing a nonlinear controller as done in [9]. Figs. 9(B) and 10(B) show the desired and actual position of the UAV, along with the actuator outputs while following the waypoints and while tracking the trajectory, respectively, for the B-mode flight.

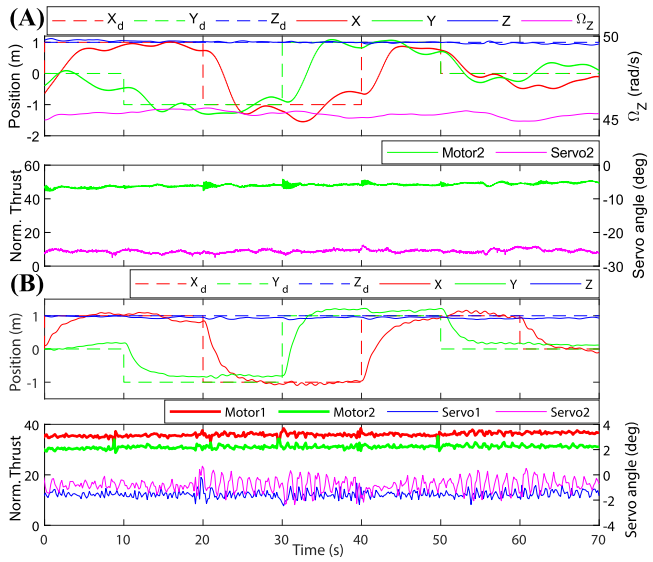

Fig. 9. Square shaped waypoint tracking with actuator outputs for (A) M-mode flight (RMS = 0.214), and (B) B-mode flight (RMS = 0.194). Take-off part has been truncated.

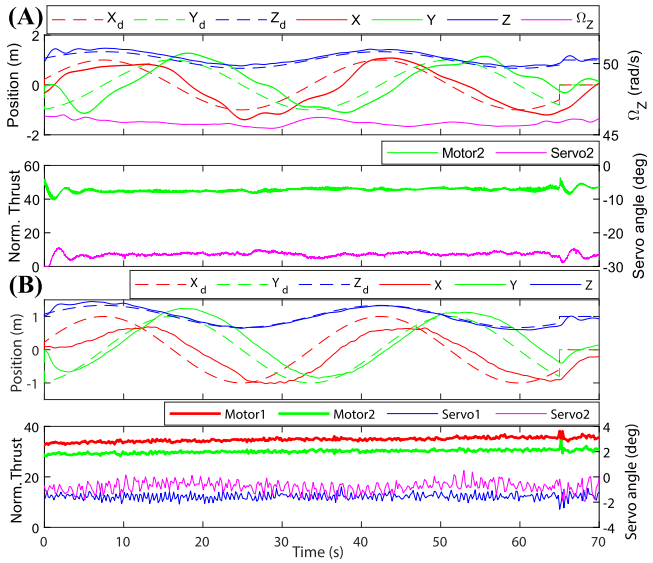

Fig. 10. Circular trajectory tracking with actuator outputs for (A) M-mode flight (RMS = 0.176), and (B) B-mode flight (RMS = 0.134). Take-off part has been truncated.

From the graphs, it can be observed that the B-mode has better control over the position compared to the M-mode. A comparison of Fig. 9(A) and 9(B) shows that B-mode can reach the waypoints and hold position better compared to M-mode. Likewise, Fig. 10(B) shows that the transient motion of B-mode is better compared to M-mode depicted in Fig. 10(A) (in particular, between 20 and 40 seconds, the roughness of M-mode motion can be observed). Although, B-mode portrayed some delay in response in the X-axis. This is due to the aerodynamic force affecting the wing and flap surfaces while moving in that direction. This is a trade-off effect that can be reduced by optimizing

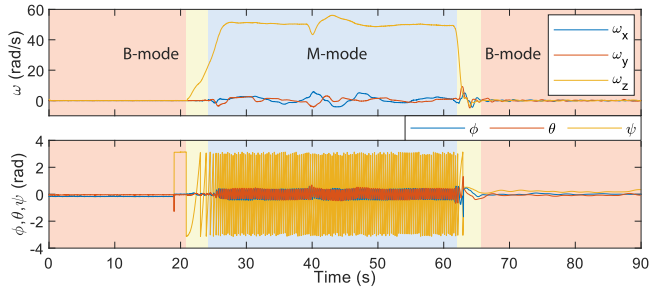

Fig. 11. Angular velocity and attitude plot during transition from B-mode → M-mode → B-mode.

the shape of the wing and flap to obtain minimum surface area facing the wind while providing the best lift while rotating in the M-mode. Comparing the Root Mean Square (RMS) values for the position tracking while following square shape waypoints for the two modes, the B-mode performed 19.49% better, whereas for the circular trajectory this performance was 36.59% better. Overall, the constant spinning nature of the M-mode affected the translational motion and hovering of the UAV, whereas the steady nature of the B-mode helped it achieve better translational motion as well as position holding after reaching the waypoints.

B. Transition Between the Two Modes

Due to the completely different nature of the flight style of both modes, the blended transition plays a crucial role in switching the modes. The transitions between the two flight modes were tested and observed. During the transition from B-mode to M-mode, it was found that the UAV can reliably switch, although losing altitude since M-mode relies on the lift produced by the wing and spinning nature of the UAV to gain altitude. In the transition from M-mode to B-mode, the stalling of the UAV was found useful to reduce the rotational speed, although the UAV takes some time to recover after entering the B-mode. An iterative approach based on the results obtained was adopted to tune the switching function parameters defined in (14).

Several factors weigh-in for the success or failure of a transition. The natural autorotation of the monocopter requires a certain distance to start, which is proportional to its weight and size. Therefore, the rate at which the motors start assisting the spins to enter M-mode impacts the success or failure of the transition from B-mode to M-mode. On the other hand, once the wing is stalled, the pitch angle can start to either decrease or increase. The first scenario is favourable, however, beyond a certain angle, the latter scenario makes the transition unstable. Furthermore, as the rotational speed is decreased to enter B-mode, the UAV has a tendency to fall inwards due to the gravity and location of the CG. Both factors can affect the success or failure of transition from M-mode to B-mode.

Fig. 11 depicts the angular velocity and the attitude of the UAV during the transition. The red shaded and blue shaded regions depict the B-mode and M-mode, respectively. A slight disturbance was experienced around 40 seconds into the flight,

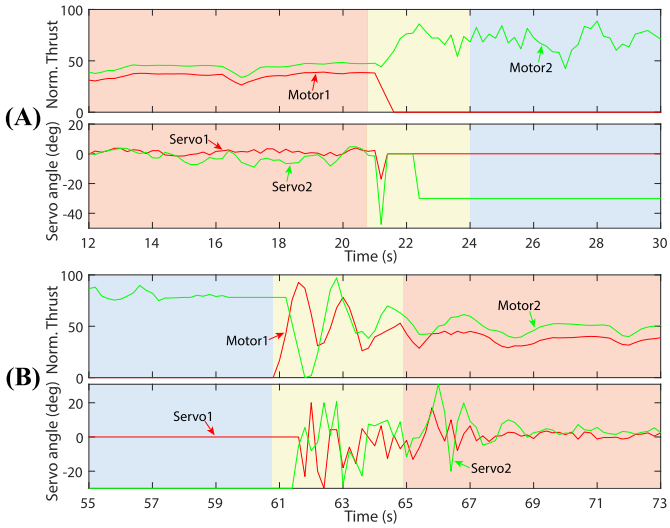

Fig. 12. Actuator output during transition from (A) B-mode → M-mode, and (B) M-mode → B-mode. The data was recorded at 4 Hz.

which can be ignored. Fig. 12 depicts the actuator outputs during the transition from one mode to another, zooming in on the transition parts.

V. Conclusion

This paper presented a novel transition strategy and control of a single-wing rotorcraft, that can fly in two different modes namely the M-mode (based on monocopter platform) and B-mode (based on bicopter platform). The rotorcraft can take off and land in both modes, as well as perform mid-air transitions from one mode to another. This novel platform utilized two actuators for flight in M-mode and utilized all four actuators for a stable flight in B-mode. The UAV can achieve better position and attitude control while flying in B-mode, whereas it can utilize the M-mode for hovering to conserve battery. The M-mode can also be utilized for using a LiDAR sensor for 3D mapping of the environment, and in case of power failure, it can help descent safely using the inherent autorotation capability. Also, a contemporary approach developed allowed the control of the angular velocity of the UAV while hovering in M-mode. Experimental proof has been presented for the position control of the UAV in both flight configurations. Based on the results, the UAV is fully controllable in both modes, having more control in the bicopter flight mode. Along with the position control, relevant data showing the transition from one mode to another was presented. The blending and transition methodology implemented produced promising results, confirming the viability of the platform to switch modes of flight mid-air. By combining the spinning monocopter platform with a stable bicopter platform, this UAV has shown more potential for real-world applications, compared to the other works done previously on these platforms.

The future work includes a more robust and reliable transition methodology. An optimal transition sequence by minimizing a cost function will be designed for better control during the transition.

References

[1] C. Papachristos, K. Alexis, and A. Tzes, "Model predictive hovering-translation control of an unmanned Tri-TiltRotor," in *Proc. IEEE Int. Conf. Robot. Automat.*, 2013, pp. 5425–5432.
[2] J. E. Low, L. T. S. Win, D. S. B. Shaiful, C. H. Tan, G. S. Soh, and S. Foong, "Design and dynamic analysis of a transformable hovering rotorcraft (thor)," in *Proc. IEEE Int. Conf. Robot. Automat.*, 2017, pp. 6389–6396.
[3] H. Jia et al., "A quadrotor with a passively reconfigurable airframe for hybrid terrestrial locomotion," *IEEE/ASME Trans. Mechatronics*, early access, Apr. 22, 2022, doi: 10.1109/TMECH.2022.3164929.
[4] P. Pounds and S. Singh, "Samara: Biologically inspired self-deploying sensor networks," *IEEE Potentials*, vol. 34, no. 2, pp. 10–14, Mar./Apr. 2015.
[5] S. K. H. Win, L. S. T. Win, D. Sufiyan, G. S. Soh, and S. Foong, "An agile samara-inspired single-actuator aerial robot capable of autorotation and diving," *IEEE Trans. Robot.*, vol. 38, no. 2, pp. 1033–1046, Apr. 2022.
[6] S. K. H. Win, L. S. T. Win, D. Sufiyan, G. S. Soh, and S. Foong, "Dynamics and control of a collaborative and separating descent of samara autorotating wings," *IEEE Robot. Autom. Lett.*, vol. 4, no. 3, pp. 3067–3074, Jul. 2019.
[7] J. Houghton and W. Hoburg, "Fly-by-wire control of a monocopter," *Massachusetts Inst. Technol.*,, Project Report,2008.
[8] E. R. Ulrich, D. J. Pines, and J. S. Humbert, "From falling to flying: The path to powered flight of a robotic samara nano air vehicle," *Bioinspiration biomimetics*, vol. 5, no. 4, 2010, Art. no. 045009.
[9] H. Bhardwaj, S. K. H. Win, L. S. T. Win, D. Sufiyan, and F. Shaohui, "P.I.D. based sliding mode control of asynchronous multi-actuator monocopter," in *Proc. IEEE/ASME Int. Conf. Adv. Intell. Mechatronics*, 2021, pp. 239–246.
[10] S. Jameson et al., "Lockheed Martin's samarai nano air vehicle: Challenges research and realization," in *Proc. 50th AIAA Aerosp. Sci. Meeting*, 2012, pp. 1–21.
[11] B. H. Kim et al., "Three-dimensional electronic microfliers inspired by wind-dispersed seeds," *Nature*, vol. 597, pp. 503–510, 2021.
[12] C. H. Tan, D. S. bin Shaiful, E. Tang, J.-Y. Khaw, G. S. Soh, and S. Foong, "Flydar: Magnetometer-based high angular rate estimation during gyro saturation for SLAM," in *Proc. IEEE Int. Conf. Robot. Automat.*, 2020, pp. 8532–8537.
[13] M. Ng, Z. M. Er, G. S. Soh, and S. Foong, "Aggregation functions for simultaneous attitude and image estimation with event cameras at high angular rates," *IEEE Robot. Automat. Lett.*, vol. 7, no. 2, pp. 4384–4391, Apr. 2022.
[14] W. Xu, Y. Cai, D. He, J. Lin, and F. Zhang, "Fast-lio2: Fast direct lidar-inertial odometry," *IEEE Trans. Robot.*, vol. 38, no. 4, pp. 2053–2073, Aug. 2022.
[15] A. Sanchez, J. Escareno, O. Garcia, and R. Lozano, "Autonomous hovering of a noncyclic tiltrotor UAV: Modeling, control and implementation," *IFAC Proc. Volumes*, vol. 41, no. 2, pp. 803–808, 2008.
[16] Q. Zhang, Z. Liu, J. Zhao, and S. Zhang, "Modeling and attitude control of bi-copter," in *Proc. IEEE Int. Conf. Aircr. Utility Syst.*, 2016, pp. 172–176.
[17] Y. Qin, W. Xu, A. Lee, and F. Zhang, "Gemini: A compact yet efficient bi-copter UAV for indoor applications," *IEEE Robot. Automat. Lett.*, vol. 5, no. 2, pp. 3213–3220, Apr. 2020.
[18] C. Blouin and E. Lanteigne, "Pitch control of an oblique active tilting bi-rotor," in *Proc. IEEE Int. Conf. Unmanned Aircr. Syst.*, 2014, pp. 791–799.
[19] B. Settle and T. Wise, "Bell Eagle Eye TR-911X–Tiltrotor unmanned aerial vehicle: Recent developments, autoland integration, and flight test demonstrations," *Annu. Forum Proc.-Amer. Helicopter Soc.*, vol. 56, no. 1, pp. 306–319, 2000.
[20] H. R. Stone and G. Clarke, "The T-wing: A VTOL UAV for defense and civilian applications," University of Sydney, 2001.
[21] V-22 Osprey Backgrounder. *Wayback Machine Internet Archive. Boeing Defense, Space & Security*, Feb. 2010.
[22] S. Bai, Q. He, and P. Chirarattananon, "A bioinspired revolving-wing drone with passive attitude stability and efficient hovering flight," *Sci. Robot.*, vol. 7, no. 66, 2022, Art. no. eabg5913.
[23] G. J. Leishman, *Principles of Helicopter Aerodynamics*. Cambridge, U.K.: Cambridge Univ. Press, 2006.
[24] H. Semat and R. Katz, "Physics, chapter 11: Rotational motion (the dynamics of a rigid body)," *Robert Katz Publications*, p. 141, 1958.
[25] L. S. T. Win, S. K. H. Win, D. Sufiyan, G. S. Soh, and S. Foong, "Achieving efficient controlled flight with a single actuator," in *Proc. IEEE/ASME Int. Conf. Adv. Intell. Mechatronics*, 2020, pp. 1625–1631.
[26] D. Brescianini, M. Hehn, and R. D'Andrea, "Nonlinear quadrocopter attitude control," Tech. Rep. 9970340, ETH Zurich, 2013.